Characterization of Liquid Refrigerant Flow Emerging from a Flooded R-123 Evaporator Tube Bundle

William Asher[1], Steven Eckels[1]
[1]*Department of Mechanical and Nuclear Engineering, Kansas State University, Manhattan, KS, USA*

The distribution of liquid droplets emerging from an evaporator tube bundle is characterized for low-pressure refrigerant R-123 with a triangular tube arrangement of pitch 1.167. The purpose of this research is to improve the understanding of the droplet ejection process to aid in the design of evaporators typically used in larger chiller systems. A laser and camera system in a shadowgraphy arrangement captured images of the evaporator headspace at varying conditions. Conventional shadowgraphy techniques were applied to recognize droplets and match droplets for velocity calculations. The evaporator conditions were varied with mass fluxes from 3.5 to 40.7 kg/s-m^2 (2250 to 30000 lb/hr-ft^2), top-rows heat fluxes from 5.3 to 31.5 kW/m^2 (1700 to 10000 Btu/hr-ft^2), and outlet saturation temperatures of 4.4 and 12.8 °C (40 and 55 F). Conditions ranged from flooded to dryout on the top rows. Particle number count, size distribution, and velocity are presented. The experimentaly measured liquid volume fraction in the headspace is also presented. Liquid distribution in the headspace is found to be a strong function of all varied properties, particularly mass flux, liquid level, and saturation temperature. The high liquid-vapor density ratio of R-123 and corresponding high velocities make it particularly difficult to separate liquid droplets before they escape the tube bundle.

Introduction

Control of liquid carryover in evaporators is a significant design issue in most larger refrigeration systems with shell-and-tube evaporators. Achieving control means understanding the mechanisms that form liquid drops and the forces that cause migration of liquid droplets out of the evaporator. Two primary mechanisms are assumed to play a role in the formation of droplets. First, high vapor velocity causes shear in the bundle that entrains droplets into the flow. Second, depending on liquid distribution within the bundle a liquid layer may exist above the bundle. In this case, wave breakup will occur above the bundle, forming and entraining droplets into the vapor flow. The migration of the liquid drops is thought to be controlled by aerodynamic forces, gravity, and droplet morphology once in the evaporator headspace. Gas velocity in the bundle is crucial and depends primarily on the refrigerant used and the capacity of the chiller. For example,

with the low-pressure refrigerant R-123, a vapor velocity of 15 m/s in the gaps between tubes can be found which can lift droplets of millimeter size, while a refrigerant such as R-134a will only have a velocity of 1 m/s for the same conditions. The vapor leaving the top of the bundle slows as it diffuses into the headspace and larger sized droplets fall back onto the top of the bundle. This may even be seen as a frothy liquid on top of the bundle. Another important factor in the droplet morphology is evaporation of liquid in the headspace dictated by the thermodynamic conditions of the flow. It is possible to have slightly superheated vapor and droplets in the flow field leaving the top of the bundle. In this case, the droplets will slowly evaporate as they flow away from the bundle. Finally, the droplets may coalesce into larger droplets and fall back into the bundle. Accurate experimental data would provide the means to understand the relative importance of the aerodynamic forces, thermodynamics (heat transfer), and wave breakup,enabling better headspace design.

The goal of the research project is to experimentally document the liquid droplets that emerge from the top of tube bundles under typical operating conditions. Data generated includes droplet size, velocity and position within the head space of the bundle for different operating conditions. The experimental data should provide insight into the physics that dominate the formation and movement of the liquid data. Also, the data provides critical validation data for those doing numerical simuation.

Shell-side bundle performance receives significantly less attention than other evaporation arrangements due to the large experimental facilities required to conduct such experiments. Previous studies in these types of bundle can be broken into two broad catagories. The first class of experiments is the study of local heat transfer and pressure drop as refrigerant flows through enhanced tube bundles primarly using 19.05 mm [0.75 inch] tubes with a standard pitch of 1.16. For example, Van Rooyen and Thome (2014) (2013) studied R-134a and R-236fa in enhanced tube bundles, documenting the local heat transfer coefficients and pressure drop in the bundle. Gorgy and Eckels (2013) reported similar data for R-134a and R-123 on enhanced tube bundles of standard pitch while results for variable pitch bundles from the same facility were given in Gorgy and Eckels (2016). Robinson and Thome (2004) studied R-134a, R-410A, and R-507A in a similar bundle with standard pitch. The four heat transfer studies had a saturation temperatures of 4 and 15 °C, mass flow fluxes 4 to 55 kg m^{-2} s^{-1} and heat fluxes from 15 to 70 kW m^{-2}.

The second class of experiments done on this standard rectangular bundle is visulizaiton documenting the flow paterns within the bundle. van Rooyen, Agostini et al. (2012) used a clear dummy tube with a digital

high-speed video camera and a laser light/photodiode and pressure drop measurement to predict the internal flow patterns Eckels and Schlup (2017) also reports flow patterns in an enhanced tube bundle using a borescope and complementing experimental data with a numerical analysis. The development of flow pattern maps from flow vizulizaiton data has been attempted in a number of studies (Grant and Chisholm 1979, Kondo and Nakajima 1980, Ulbrich and Mewes 1994, Cheng, Ribatski et al. 2008). A characteristic of the bundle flow is a region of droplet entrained flow at the top of the bundle in the dryout region. The fate of these entrained drops in the head space above the bundle has not been documented in literature and is the main aim of this paper.

The current study uses a shadowgraphy technique to characterize droplets. In this method, a pulsed backlight is used in the head space. An image of a particle, based on the difference in refractive index between the object being imaged and the surrounding medium, is recorded. Specifically, the light source illuminates the object, and the area that the camera sees consists of a bright background with dark areas corresponding to the object boundaries. A pulsed shadowgraph is one in which the background is illuminated only at the time the picture is recorded. The specific details of this imaging method are described in Castrejón-García, Castrejón-Pita et al. (2011) and Kashdan, Shrimpton et al. (2003). Image processing techniques are used to detect the edge of the particle from the shadow picture and convert this into an actual size. This imaging method has been used to calculate particle size in two phase flows in a number of geometries (Dai, Chou et al. 1998, Hay, Liu et al. 1998, Patruno, Marchioro Ystad et al. 2010). In Patruno, Marchioro Ystad et al. (2010), shadowgraph photography was used specifically to image entrained droplets in two-phase annular flow in a tube.

The paper presents the unique experimental facility developed to measure the droplet size, velocity and count in the headspace of an R-123 enhanced tube bundle. This includes both the bundle system and the optical system. The techniques used to determine droplet size and velocities are also presented. The bundle flow parameters such as mass flux and average bundle heat flux are also discussed. The final section presents the experimental results and a discussion of the physics involved.

Facility Description

The flooded evaporator test section with clear optical sight glasses is the central component of the system as shown in Figure 1. The refrigerant circulation is maintained by a pump and thus operates at a single pressure and is described in the next section. Two water loops are used to supply energy for boiling the refrigerant while condensation is accomplished with cold glycol. This section also describes the optical equipment used in the shadowgraphy technique.

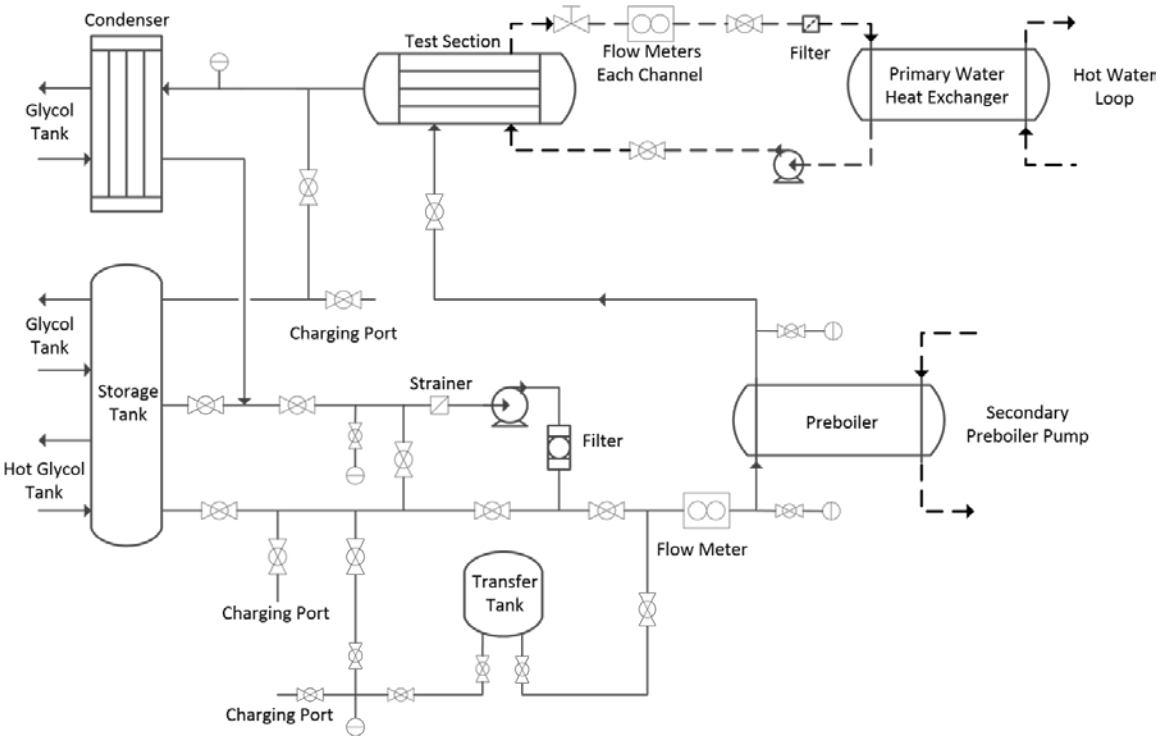

Figure 1: Schematic of Test Facility

Refrigerant Loop

Figure 1 shows the refrigerant leaving the test section to be condensed in a large brazed plate heat exchanger. Minimizing the pressure drop between test section and condenser is critical for a low pressure refrigerant. In this case, a large vapor line 7.6 cm (3 in) refrigerant line and condenser inlets are used. The maximum load on the condenser is 81 kW (23 ton).

The refrigerant pump is a magnetically driven gear pump with a capacity of 1.3 L/s (21 GPM) and delivers up to 1551.3 kPa (225 PSI) maximum pressure. The refrigerant pump in located 3 m (10 ft) below

the bundle entrance in a pit and the NPSH is maintained by a static liquid head. A storage tank is installed parallel to the condenser allowing adjustment of the refrigerant charge for each test point. A filter dryer is used upstream of the pump and is primary for moisture control. A coriolis type flow meter measures liquid refigerant flow rate (±0.1% of rate). Pressure is measured through out the loop with standard strain gauge pressure transducers (±0.15% FS) and temperature with calibrated thermisters (±0.1 °C). Degassing of the refrigerant loop is accomplished with the storage unit and test section set in natural circulation mode with a temperature difference to drive condensation and accumulation of air at the highest point in the system.

Test section primary and pre-boiler water circuit

The pre-boiler is a shell and tube heat exchanger; the refrigerant circulates in the tubes (two passes), and the heating water circulates in the shell, while the test section is of the oposite arragnement. Both water loops that suppy energy for evaporation have a water pump, flow meter, filters, and secondary heat exchanger. The water pumps are 2.2 kW (3 HP) centrifugal pumps, and every flow meter is a coriolis type flow meter. A secondary heat exchanger in each loop provides heat to the primary circuit from the warm water tank.

Test Section

The central part of the test facility is the bundle test section shown in Figure 2. The bundle holds 24 tubes in a triangular pitch with a P/D of 1.167 (20 active tubes, 4 dummy tubes, and one slot for inlet refrigerant distribution). The two-phase refrigerant mixture from the pre-boiler is distributed at the bottom of the bundle by four inlet tubes that come in through the bottom of the bundle and are capped with 8 downward facing tubes (downward facing u-tubes at top of each inlet). The active heat transfer area consists of 20 tubes in 5 circuits. These tubes are enhanced 3-D tubes with internal enhancements having a nominal outer diameter of 19.05 mm (0.75 inch) and inner diameter of 15.88 mm (0.63 inch). The water flow rate in each circuit is measured with coriolis type meters (±0.1% of rate). Inlet and outlet water temperaure of each tube are measured with thermistors (±0.1 °C). Where needed, half dummy tubes are mounted to the sides of the bundle to provide a realistic boundary conditions as shown in Figure 2. Finally, the bundle is 1.0 m (39.4 inch) long in order to minimize the end effects.

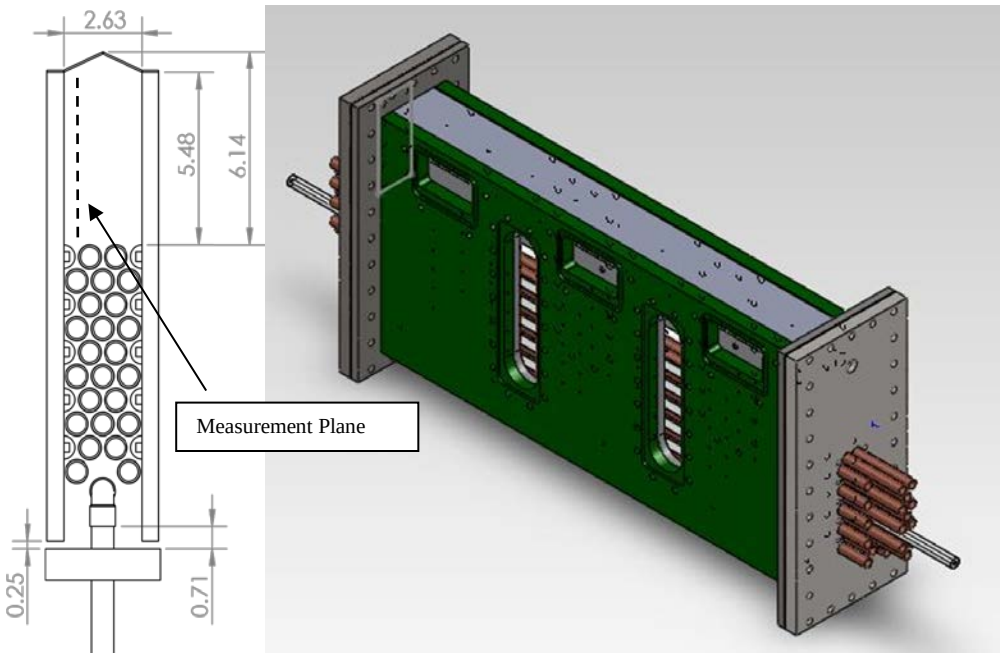

Figure 2: Schematic of Test Section

The test section is a rectangular pressure vessel that is essentially a shell and tube heat exchanger; the refrigerant flows upwards across the tube bundle while water circulates in the tubes. The test section accomodates both high and low pressure refrigerants. Its inner dimensions are 0.4254 m (16.75 inch) high, 98.4 mm (3.875 inch) wide, and 1 m (39.37 inch) deep. Inserts reduce the width of the test section to 66.7 mm [2.63 inch]. The 24 tube bundle is placed as low as possible in the shell to allow maxiumum measurement space. A distribuiton plate is used at the top of the bundle to induce a measured pressure drop that helps balance vertical flow in the bundle. Flow exits after the distribution plate through six ports on the side of the test section to the condensor. The test section also includes four large sight glasses to provide clear view ports into the bundle centered on 1/3 spacing of the bundle length.

Optical System

A schematic of the shadowgraphy system is shown in Figure 3. This system is composed of components common to PIV and particle sizing systems, namely a light source and camera. An Nd:YAG laser generates the dual pulse used to determine velocity. The spacing of the pulses is based on the expected maximum velocity and ranges from 240 to 1100 μs, with an uncertainty of 10 ns. The analysis and ultimatly the accuracy of the backlight system depends on the uniformity of the light as seen by the camera. The current system use

an attenuator and holograph diffuser to backlight the 76 mm (3 inch) by 125 mm (4 inch) viewing window. Two sets of optics are used on the cameral (100 mm and 50 mm focal length lenses) allowing fields of view of approximately 50 mm and 100 mm respectivitly. The lower magnificaiton lens has the advantage of visulizing the entire crosssection of the bundle head space window while the higher magnification lens allows for the capture of smaller droplets. The camera is mounted on a horizontal Vernier stage with 0.1 mm markings for precise location of the focal plane across the bundle width. The high resolution CCD camera and associated imaging optics (lenses) connect with the droplet size and velocity vector analysis software.. The image pairs generated by the system require multiple analysis steps before droplet size, distribution, and matched particle velocity are determined. The following section outlines the analysis required.

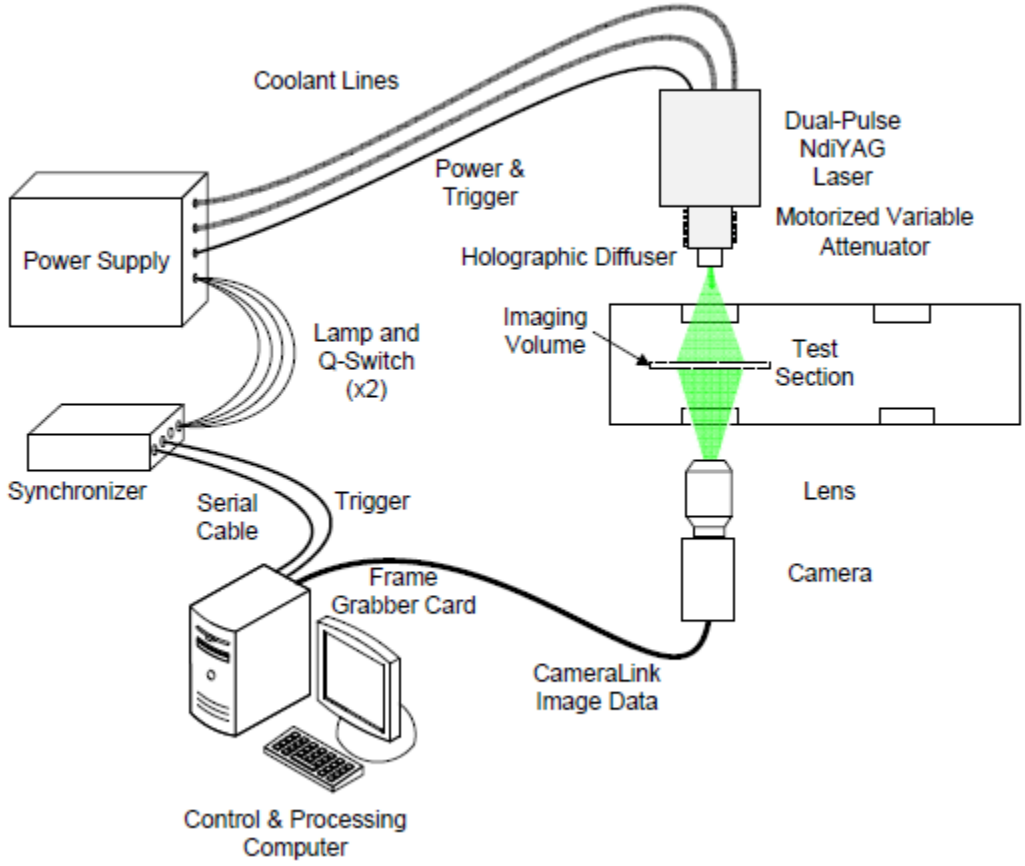

Figure 3: Schematic of Optical System

Image Analysis

For any droplet imaged, three main quantities are desired: droplet diameter, position, and velocity. All properties of a droplet are quantified by the capture software. Droplet diameter is the defined by the projected area diameter and is based on the pixels recognized inside the droplet shadow. In other words, $D_{droplet} = \sqrt{4 * A_{pixels}/\pi}$. Position is height of a droplet centroid referenced to top of the uppermost tubes in the bundle in units mm. Velocities reported are the vertical components of velocities, though horizontal velocities are recorded but not used for the presented data. Velocities are calculated as the droplet shift centroid-centroid between image pairs divided by the time step between each image of the pair.

Image Processing

To make it possible to recognize droplets through the capture software, each image was manipulated to highlight the captured droplets from the background. There are five main steps to this procedure: scaling, intensity inversion, background subtraction, filtering, and masking. A script was written to scale each pixel in an image such that the highest intensity pixel is at the maximum intensity possible for a 12-bit image of 4095.

Further manipulation of images was carried out within the capture software. An example of an image at this stage in the process is shown in Figure 4(a). As the software used thresholding to recognize droplets, a greyscale inversion was carried out to make the background dark and droplets bright. An average background image was then created from each run of 100 image pairs that was then subtracted from each image in that run. Following the background subtraction, a local median filter of 3 pixels size was used to more sharply define droplets. A multiplier of 5 was then applied to each pixel and then an image mask was used to set pixels with an intensity less than 1000 to 0. Images at this point were ready to have droplets recognized.

Droplet Recognition

Droplet recognition occurs in two main steps: particle sizing and particle matching. Particle matching takes the pre-processed images and determines all possible droplets by use of thresholding. For our processing, the threshold was set to 999. As the images were previously manipulated to mask all areas with an intensity below 1000, this means any visible pixels on our pre-processed images were available to the sizing kernel.

The particle sizing kernel was allowed to recognize droplets from as small as 2 pixels up to as large as 70 and 156 pixels for the 50 mm and 100 mm lenses, respectively. The upper limit corresponds to a maximum droplet diameter of approximately 4000 μm. Furthermore, to filter out possible non-droplets like liquid structures on the inner glass wall, droplets were limited to a circularity from 0.4 to 2 to favor recognizing the more circular droplets. A droplet's circularity is defined by $Circularity = 4 \cdot Area/Perimeter^2$.

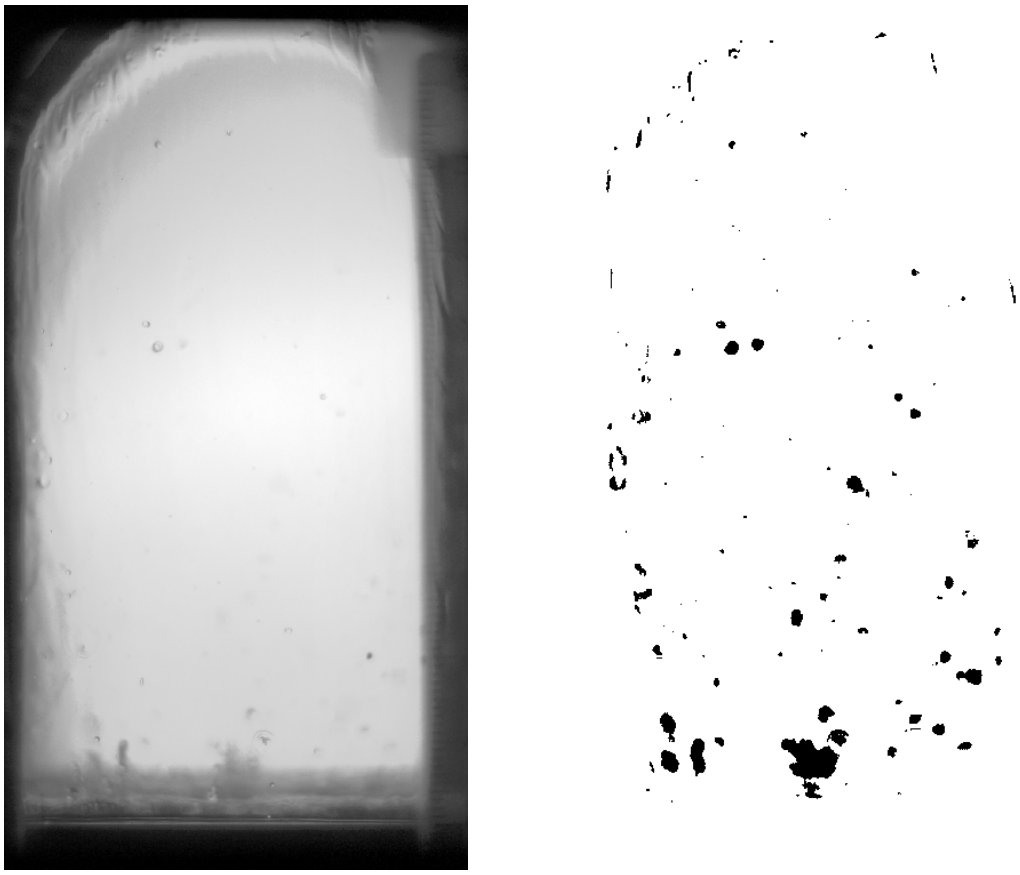

(a) (b)

Figure 4: (a) Unprocessed capture image. (b) Processed image. Inverted to highlight droplets.

Particle matching allows for the setting of the maximum allowable particle shift. As stated previously, timing settings were set based on an expected maximum droplet velocity and a shift of ±30 pixels both vertically and horizontally. Droplets were allowed a maximum size difference between images in a pair of 35%. As droplet motion for a bundle includes both rising and falling droplets, no local motion match or neighborhood particle matching algorithms were used.

An example of the end result of image processing is shown in Figure 4(b). The image has been inverted for the purpose of this paper to highlight the droplets. Non-white pixels (at least in the image shown) would be subject to both particle recognition and matching.

Calibration

Three main types of calibration images were taken with this data. Representative images are shown in Figure 5 below. A calibration target normally used for distortion calibration was used as a check of the droplet recognition & matching ability of the software. This target, shown in Figure 5(a) has opaque circular dots with diameters from 62.5 to 1000 μm and spacings from 125 to 2000 μm. Results of this check show an uncertainty in droplet diameter of ±21 μm for droplets larger than 100 μm using the 50 mm lens and ±11 μm for droplets larger than 50 μm using the 100mm lens.

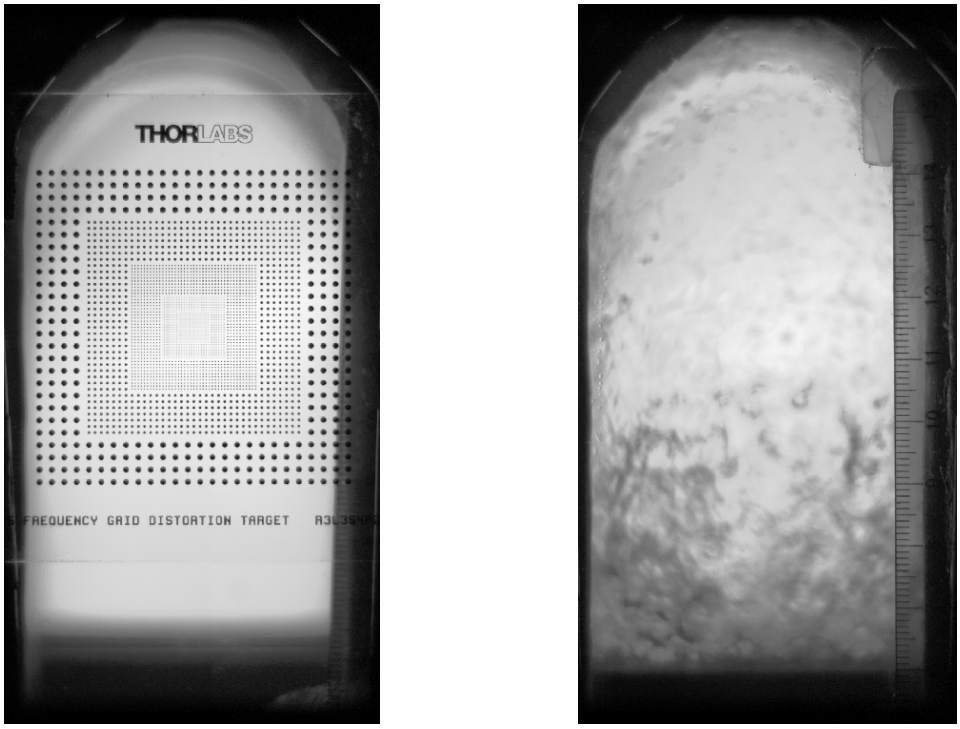

(a) (b)

Figure 5: (a) Calibration target for sizing uncertainty. (b) Calibration image for focusing on outer wall.

A calibration image was also taken for each liquid level and lens in an experiment. A representative image for the 50 mm lens is shown in Figure 5(b). The horizontal Vernier stage is set to a position of 0 mm and then the lens is focused on a clear plastic ruler with opaque spacing lines & text. The text & lines are

located against the exterior wall of our outer test section sight glass, so focusing on the ruler means we are focused on the outer wall. The center of the bundle is located 69.9 mm inward from the outer window of the bundle, between the two top tubes. This is image plane L. Positions J and K are located 22.2 and 11.1 mm towards the camera from the bundle center, respectively. Positions M and N are located 11.1 and 22.2 mm away from the camera from the bundle center, respectively. Positions J and N are both located between a tube and a half tube while positions K and M are located above the top two tubes.

A final set of calibration images (not shown) is taken at the inner wall to determine the height of the top of the bundle relative to the camera image. The Vernier stage is set to 36.5 mm and the bundle is front-lit to expose the half tubes seen in the left diagram of Figure 2. The flat side of the aluminum half-tubes are in focus and the top corresponds to the top of the bundle.

Bundle Calculations

The focus of this study is the headspace droplet distribution and morphology, but it is important to tie those properties to typical operating conditions within a bundle evaporator. Parameters such as mass flux, heat flux, and exit quality describe or are an effect of our operating conditions. In this section the equations used to calculate those parameters are presented , as well as the uncertainties associated with those conditions.

Mass Flux

Mass flux is determined from the measured mass flow rate and the physical parameters of our bundle. It is important to note that mass flux for a bundle is generally defined based on the minimum area encountered in the bundle. From our nominal outer tube diameter of 19.05 mm (0.75 inch) and pitch-diameter ratio of 1.167, this gives a minimum gap of 3.175 mm (0.125 inch) between adjacent tubes. For our bundle, each row has three gaps or the equivalent and our rows are 1 m (39.37 inch), yielding a fluid cross-sectional area of 9525 mm^2 (14.76 $inch^2$). This can be expressed by

$$G = \frac{\dot{m}}{A_c} \tag{1}$$

with mass fluxes ranging from 3.5 kg/m^2 s (2250 $lb/hr\ ft^2$) to 40.7 kg/m^2 s (30000 $lb/hr\ ft^2$).

Heat Flux

Heat flux is determined from the measured water temperature drop across a tube, the water flow rate from the tube, and the nominal tube outer area. Assuming pressure drop's effect on heat is insignificant, the heat and heat flux, respectively, for a given tube is

$$q_{tube} = \dot{m}_w c_{p,w}(T_{in} - T_{out}) \tag{2}$$

$$q"_{tube} = \frac{q_{tube}}{A_{tube,o}} \tag{3}$$

In terms of our bundle, the heat fluxes reported are the average of the top two rows. In other word, there is a top-rows heat flux, $q"_{top-rows}$, which is the mean of the heat fluxes of the top five tubes of the bundle. Top row heat fluxes ranged from 5.3 kW/m^2 (1700 Btu/hr-ft^2) to 31.5 kW/m^2 (10000 Btu/hr-ft^2), with the two lowest heat fluxes being the maximums sustainable for their given mass fluxes.

Exit Quality

An exit quality from the bundle was determined from the refrigerant's preboiler inlet enthalpy, the amount of heat transferred into the refrigerant in the preboiler, and the amount of heat transferred into the refrigerant in the bundle. The preboiler and bundle heat transfers are found from

$$q_{pb} = \dot{m}_w c_{p,w}\left(T_{pb,in} - T_{pb,out}\right) \tag{4}$$

$$q_{bundle} = \sum_{all\ tubes} q_{tube} \tag{5}$$

The inlet enthalpy of the refrigerant to the preboiler is calculated from REFPROP using the measured refrigerant pressure and temperature. The following equation is then used to calculate the bundle test section outlet enthalpy of the refrigerant:

$$h_{ts,outlet} = \frac{q_{pb} + q_{bundle}}{\dot{m}_r} + h_{pb,inlet} \tag{6}$$

The test section outlet enthalpy is then fed to REFPROP in the form shown in equation (7) with the test section outlet pressure to determine the quality of the refrigerant leaving the test section. Exit qualities were found to vary from 78% at higher mass fluxes to 100% with lower mass fluxes. The 78% quality is due to significant liquid carryover at higher mas fluxes.

$$X_{ts,outlet} = f(h_{ts,outlet}, p_{ts,outlet}) \tag{7}$$

Liquid Volume Fraction

It is possible from the data collected to calculate liquid volume fraction as a function of height from the experimental data. In order to do so, the depth of focus (DOF) must be calculated from our physical setup and camera and lens parameters. From the physical dimensions of our setup (distances, focal length, and camera pixel size) we calculate a DOF of 3.52 and 1.37 mm for the 50 and 100 mm lenses, respectively.

Liquid fraction is found by calculating the total liquid droplet volume per binned height of 5 mm. Droplets are assumed to be spheres with their diameter being the software-calculated projected diameter described in the Image Analysis section. For cases in which droplets span more than one bin, corrections are made using the volume formula for a spherical cap. The total liquid volume is then averaged over the 100 images that make up a set. The total bin volume is also calculated by multiplying our region of interest by the bin height and the depth of focus. So, the bin volume is given by (35 mm)·(5mm)·(DOF), where the DOF is dependent on the lens used.

The liquid volume fraction is then the ratio of liquid volume to bin volume and is placed at the center of the bin's bounds (e.g. if a bin spans from 50 to 55 mm, the liquid fraction is placed at 52.5 mm). The procedure above is used to handle droplets that span more than one bin. Equation 8 illustrates a modification of the above process wherein we find the volume-averaged droplet diameter per bin with equation 9. The form of equation 8 is useful for finding the uncertainty in our liquid fraction.

$$\phi_i = n_i \frac{\pi \overline{D}_i^3}{6H \cdot W \cdot DOF} \tag{8}$$

$$\overline{D}_i = \sqrt[3]{\frac{6V_{l,total,i}}{n_i}} \tag{9}$$

Uncertainties

Uncertainties exist both in our thermodynamic bundle parameters and in our droplet data. A quantification of uncertainties is important even when difficult to carry out. Table 1 below details known uncertainties for various measurements.

Table 1: Measurement Uncertainties		
Variable	**Uncertainty**	**Notes**
Temperature, T	+0.1 C (0.2 °F)	Thermistors
Pressure, P	+0.15% full scale	Strain gauge transducers
Flow, $\dot{m}$	+0.1% reading	Coriolis type
Depth of Focus, DOF	+0.5 mm +0.2 mm	50mm lens, 100 mm lens
Droplet diameter, D	+21 µm +9 µm	50mm lens 100 mm lens
Image pair timing, Δt	10 ns	
Droplet Count	+10% value	

The uncertainties for temperature, pressure, flow, and timing uncertainty are based on manufacturer's specifications. For both temperature and pressure, sensors were calibrated and showed uncertainties lower than what is shown in Table 1. The uncertainty for depth of focus is based on observation of our images and the understanding that out of focus droplets outside our measurement volume might be included in our results. The uncertainty for droplet diameter is statistical and based on our calibration tests involving our target shown in Figure 5(a). The droplet count uncertainty is found from a manual inspection of a sampling of images, identifying cases wherein both droplets were not counted and non-droplets were counted.

We can perform a progation of uncertainty on parameters to find the resultant uncertainty. For liquid volume fraction, the uncertainty, is given by

$$U_\varepsilon = \sqrt{\left(\frac{\partial \phi}{\partial n} U_n\right)^2 + \left(\frac{\partial \phi}{\partial \overline{D}} U_{\overline{D}}\right)^2 + \left(\frac{\partial \phi}{\partial DOF} U_{DOF}\right)^2} \tag{10}$$

Equation 10 makes use of the formula for liquid fraction given in Equation 8. Using the same procedure, the uncertanties on the bundle parameters are also calculated, resulting in ±5% for both mass flux and heat flux and in exit qualities of ±8%.

Results

A test matrix of experimental conditions was devloped to highlight the effect of saturation temperature, mass flux and top row heat flux. The range of conditions is shown in Table 2. At each point a number of runs were obtained. A run consists of 100 pairs of images from which 200 sets of droplet size and location can be obtained and 100 sets of matched droplet velocity plots.

Another important test parameter is the liquid level in the bundle. For a flooded evaporator, this can be thought of as the extra liquid sitting on top of the bundle that the vapor must pass through before

exiting the bundle. The liquid level in an actual system would be dependent on the evaporator design, headspace design and refrigerant charge level recommended by the manufacturer. For example, a low liquid level would result in dryout in the upper rows of the bundle. Based on recommendations from industry, the ideal liquid level for R-123 was set as the lowest liquid charge in the system (and thus the test section) that could be sustain before dryout of the upper tubes occurred. The storage tank connected to the system was used to transfer R-123 in and out of the test system to vary the charge. The dryout point was determined by monitoring the refrigerant side heat transfer coefficients of the upper rows. Runs of data for each setpoint in Table 2 were obtained with a high liquid level, low liquid level and optimum level.

Table 2: Experimental Test Conditions

Saturation Temperature C (°F)	Mass Flux Kg/m^2 s (lb/hr-ft^2)	Top Rows Heat Flux KW/m^2 (Btu/hr-ft^2)
4.4 (40)	20.4 (15000)	15.7 (5000)
4.4 (40)	40.7 (30000)	15.7 (5000)
4.4 (40)	40.7 (30000)	31.5 (10000)
12.8 (55)	3.5 (2250)	5.3 (1700)
12.8 (55)	10.2 (7500)	11.0 (3500)
12.8 (55)	20.4 (15000)	15.7 (5000)
12.8 (55)	40.7 (30000)	15.7 (5000)
12.8 (55)	40.7 (30000)	31.5 (10000)

Figure 6 and Figure 7 presents the baseline data for R-123 at 12.8 C (55 F) with a mass flux of 20.4 kg/m^2 s (15000 lb/hr ft^2) and an upper row heat flux of 15.7 KW/m^2 (5,000 Btu/hr-ft^2) with the 50 mm and 100 mm lens respectively. The data shown in this figures is summation of all 100 images (first image taken per image pair) taken. Velocity plots only show droplets which were matched between image pairs. Part (a) in both figures shows the total counts with matched and unmatched particles. The 50 mm lens has a larger viewing area and the 100 mm lens counts smaller particle sizes. Part (b) shows the summed particle count per 5 mm bin height above the tube. As discussed previously, the bin height for this data was set at 5 mm, with depths of focus for the 50 mm lens of 3.52 mm and 1.37 mm for the 100 mm lens. On average about 60 particles were detected in each 5 mm bin height over the sum of 100 images or on a per image bases less than 1 particle per bin. It is also important to note the differences in the two lens sizes. The 50 mm lens data drops with height while the 100 mm lens data remain constant primarily because the 50 μm droplets are resolved with the higher magnification lens. The 50 mm lens is unable to resolve droplets below ~100 μm, which are shown in for the 100 mm lens to have the highest count in the droplet size

distribution of part (c). The final graph (d) of the baseline data shows all the velocity information obtained from the 100 image pairs. R-123 as a low density refrigerant has rather high vapor velocity and is prone to liquid carry over from the bundle. This can be seen for both lenses in the velocity information. Both show a net-positive skew in the velocity, though it is more prominent with the 100 mm lens. The discrepancy between the two lenses has two explanations. The 100 mm lens captures smaller droplets more likely to be faster and carried higher in the headspace and it has a more limited field of view, limiting knowledge of the upper 30 mm of the headspace where we might see droplets dropping.

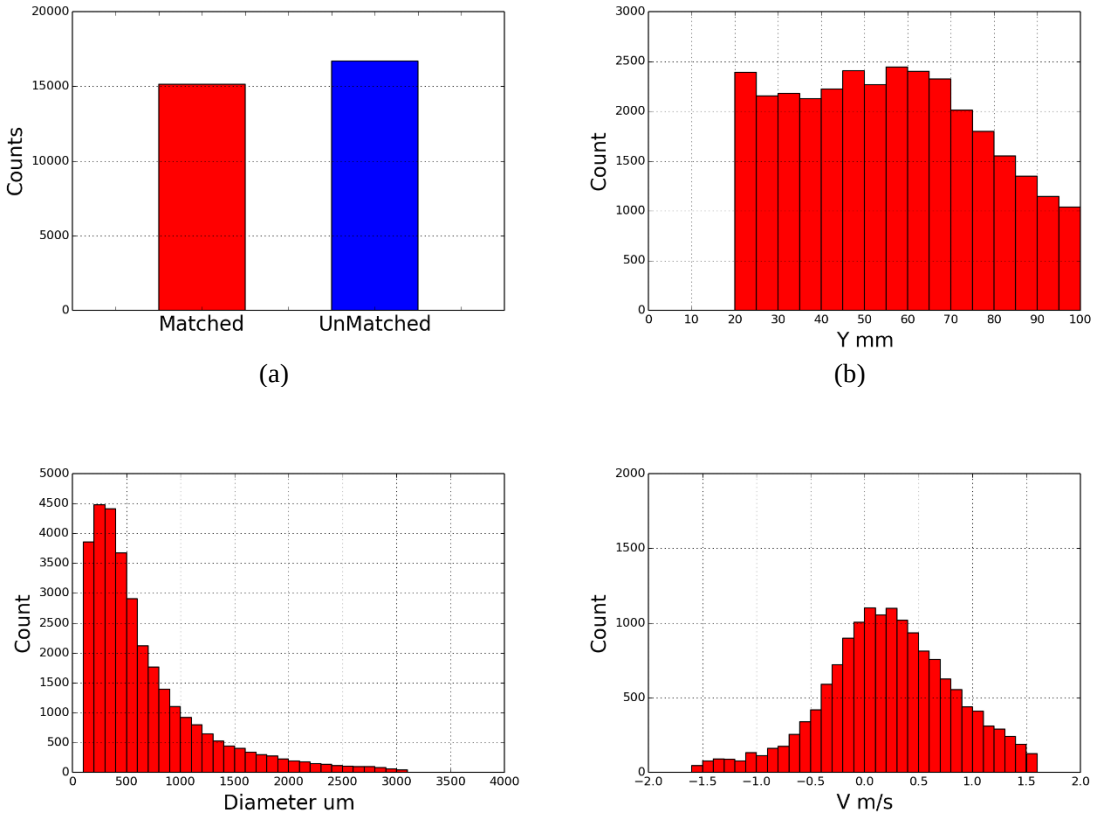

Figure 6: Data summary for 12.8 ^{o}C (55 F) at 20.4 kg/m^2 s (15000 lb/hr ft^2) with 15.7 KW/m^2 (5,000 Btu/hr ft^2) with 50 mm lens showing (a) total counts, (b) counts versus height, (c) counts versus size, and (d) velocity distribution for ideal liquid level case. All charts are summation of 100 images.

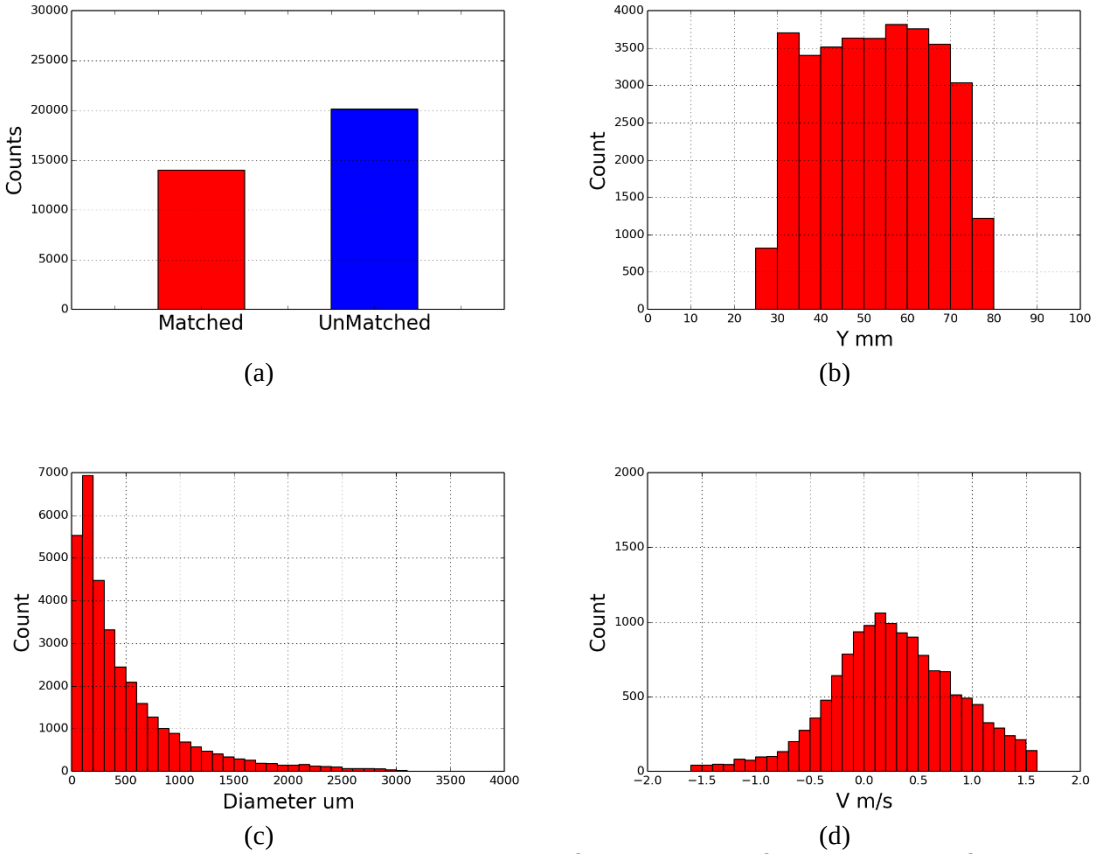

Figure 7: Data summary for 12.8 °C (55 F) at 20.4 kg/m^2 s (15000 lb/hr ft^2) with 15.7 KW/m^2 (5,000 Btu/hr ft^2) for 100 mm lens showing (a) total counts, (b) counts versus height, (c) counts versus size, and (d) velocity distribution for ideal liquid level case. All charts are summation of 100 images.

Figure 8 highlights the effect of liquid level in flooded evaporator. With R-123 it becomes difficult to term this a liquid level, as the high vapor velocities in the head space cause continual breakup and entrainment of any liquid in the headspace preventing a stable liquid level from developing. The optimal conditions (lowest system charge without dryout on the upper tube) are shown in Figure 6. Higher liquid charge conditions are shown in part (a) and (c) of Figure 8. Note that the sum of particles counts is slightly higher and a similar particle size distribution is obtained compared to the base case of Figure 6. For lower liquid levels (part (b) and (d)), the liquid counts are significantly lower and the particle size distribution has shift towards the smaller size range. All three liquid levels shows a nearly constant count versus height indicating droplets that are entrained in the vapor flow are reaching the top of bundle.

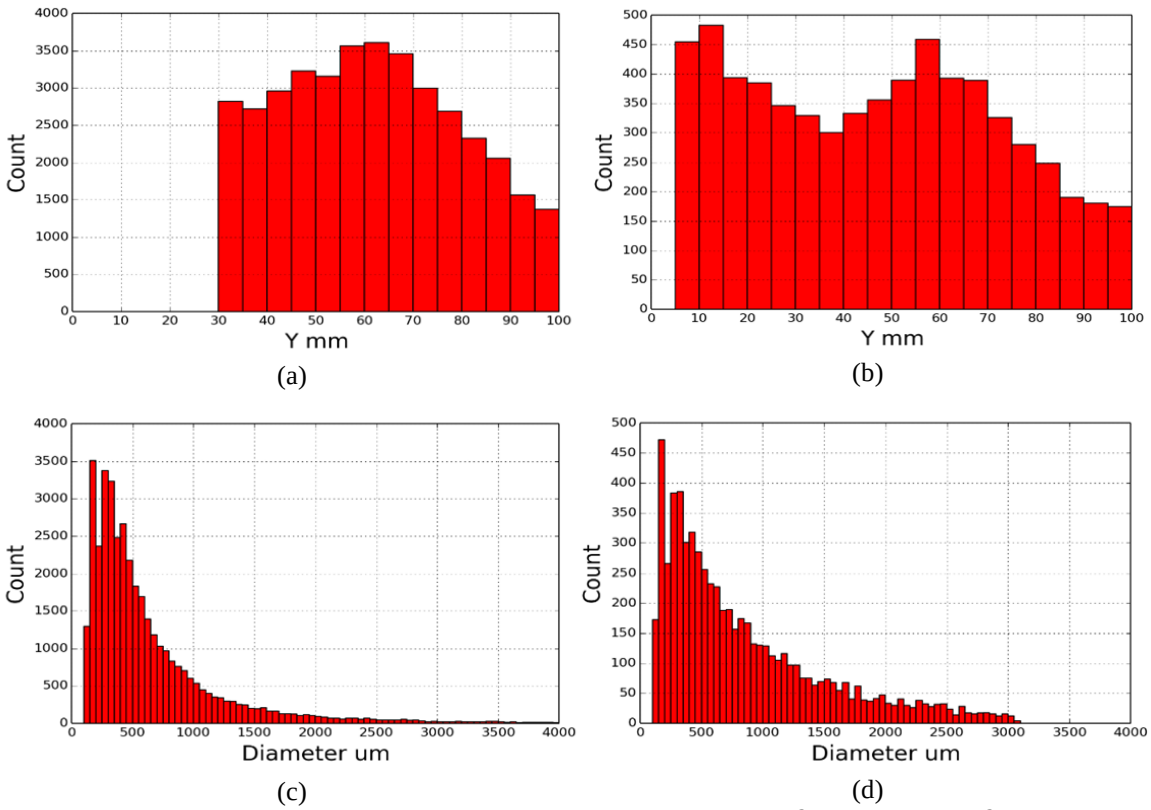

Figure 8: Data for liquid level comparison for 12.8 °C (55 F) at 20.4 kg/m^2 s (15000 lb/hr ft^2) with 15.7 KW/m^2 (5,000 Btu/hr ft^2) for 50 mm lens showing (a) high liquid level count, (b) dryout conditions counts, (c) high liquid level counts, (d) dryout counts. All charts are summation of 100 images.

Figure 9 highlights the evolution of the droplet counts as mass flux is increased. Droplet counts increase and the effect of height decreases with increased mass flux. As a reference point, mass fluxes shown in (a) and (b) give a headspace vapor velocities that are typical for medium pressure refrigerants (R-134a for example) while condition (c) is more typical of headspace conditions for low-pressure refrigerants. Note that data for the highest mass flux tested at 40.7 kg/s-m^2 (30000 lb/hr-ft^2) is not included in Figure 9. This is due to the images being too chaotic at the ideal liquid level for droplet recognition, with droplets being thrown against the glass walls and dropping down from the top of the headspace, distorting the images too severely.

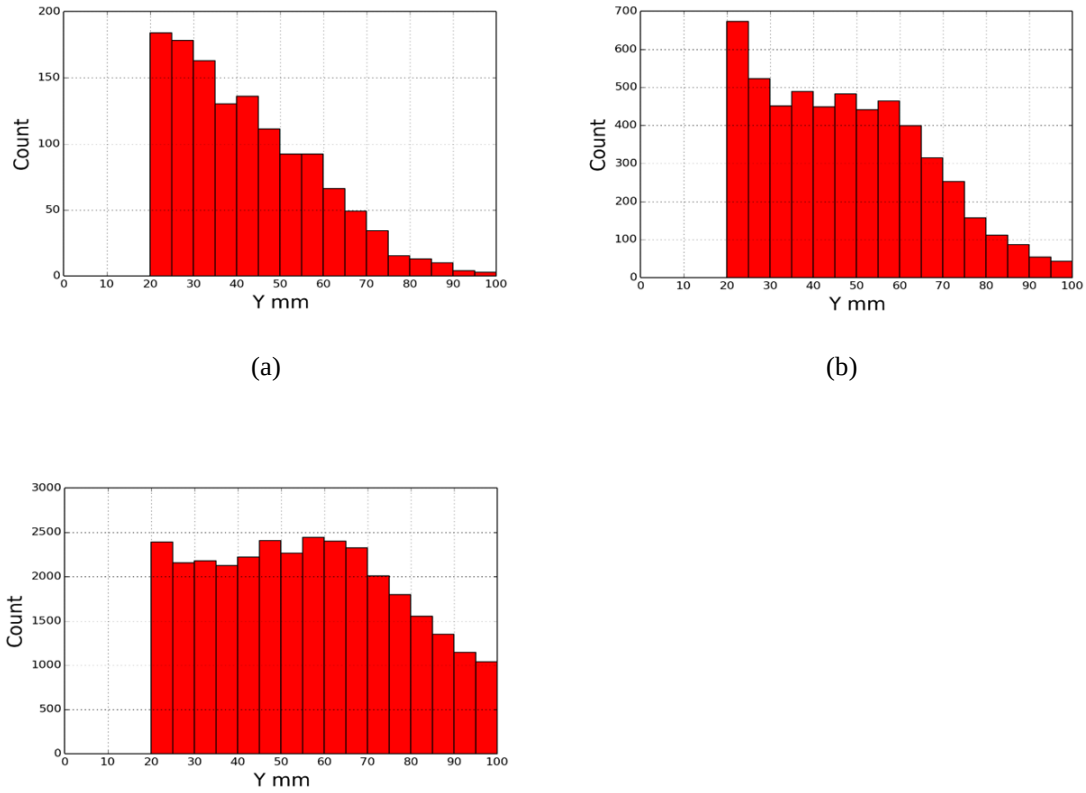

Figure 9: Data for counts versus height for different mass fluxes at 12.8 ºC (55 F) and ideal liquid level for lowest heat flux (a) at 3.5 kg/m^2 s (2,250 lb/hr ft^2), (b) at 10.2 kg/m^2 s (7,500 lb/hr ft^2), (c) at 20.4 kg/m^2 s (15000 lb/hr ft^2) All charts are summation of 100 images.

It is also interesting to see the particle size distribution as a function of height for the base case, as this helps explain the data in Figure 9. Figure 10 shows the cumulative size distribution function for five binned heights. As expected, the particle size distribution shifts towards small sizes higher in the headspace of the test section. To read this chart, consider the curves for 50 to 60 mm and 90 to 100mm.. 50% of particles are below 500 µm from 50 to 60 mm and 90% of droplets are below 1500 µm. For the 90 to 100 mm curve, 95% of droplets are below 1000 µm while nearly 100% of droplets are smaller than 2000 µm, showing how droplets tend towards a smaller diameter as height increases.

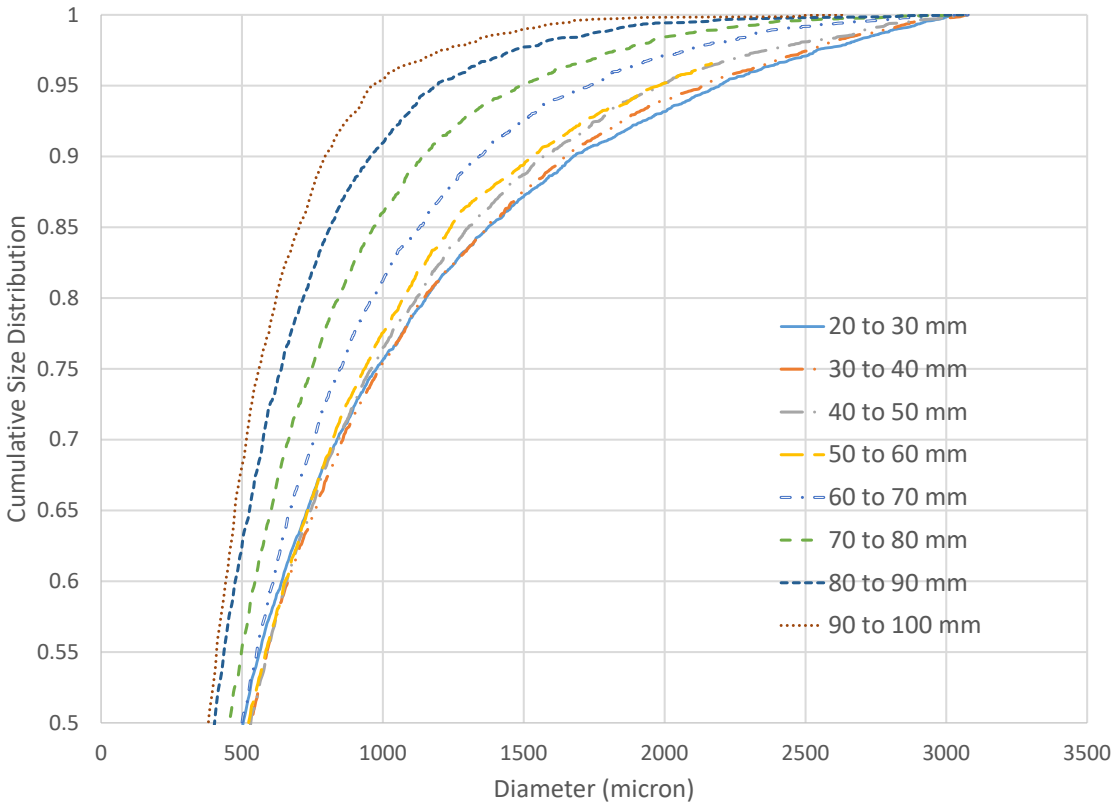

Figure 10: Cumulative fraction less versus particle size for 12.8 °C (55 F) at 20.4 kg/m^2 s (15000 lb/hr ft^2) with 15.7 KW/m^2 (5,000 Btu/hr ft^2) with 50 mm lens

The results presented in this section gives a view of the data generated with the system. As expected, optical measuring techniques generate extensive amounts of data. The goal is to not only provide data that is useful for calibration of numerical models but also provide the reader with an understanding of the data trends. To that end, perhaps the simplest way to combine the views of the data is to present the liquid volume fraction vs height, which takes into account all droplet data over both time and space for a given set of conditions. Figure 11 shows liquid fractions calculated from Equation 8. Compared are three different mass fluxes at the ideal liquid level condition. Results for the 40.7 kg/s-m^2 (30000 lb/hr-ft^2) mass flux conditions are not included as droplet images were too chaotic to achieve droplet recognition due to liquid both thrown against and dripping down the walls of the headspace.

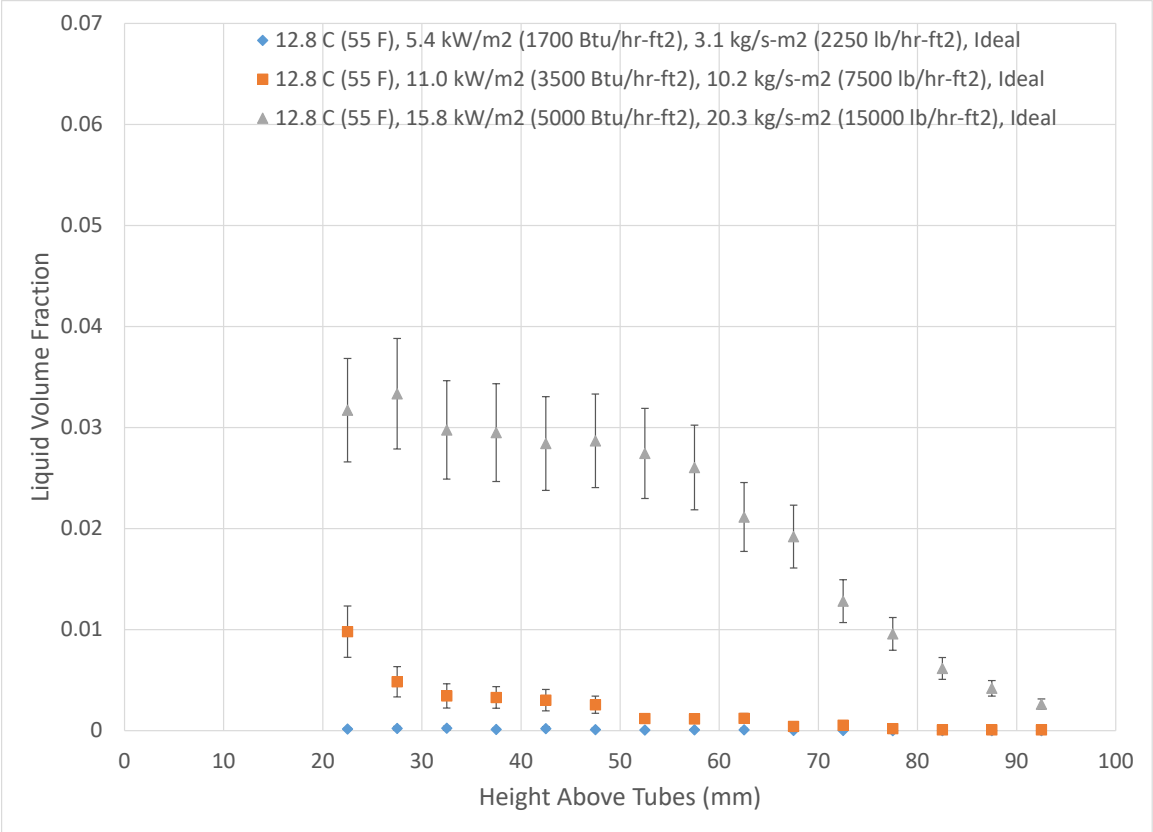

Figure 11: Liquid volume fraction versus height for 12.8 °C (55 F) at ideal liquid level with 50 mm lens for three mass fluxes

Compare the results of Figure 11 with Figure 9 cases (a), (b), and (c). For the lowest mass flux, the refrigerant is nearly all vapor throughout the entire headspace, whereas this occurs for the medium mass flux by approximately 70 mm. However, with the base case of 20.3 kg/s-m^2 (15000 lb/hr-ft^2), we are exiting the bundle with a comparatively appreciable amount of liquid, which corresponds with the skewed positive velocity distribution of Figure 6(d) and height histogram of 6(b). The results of the base case can then be compared with its corresponding dryout liquid level in Figure 12.

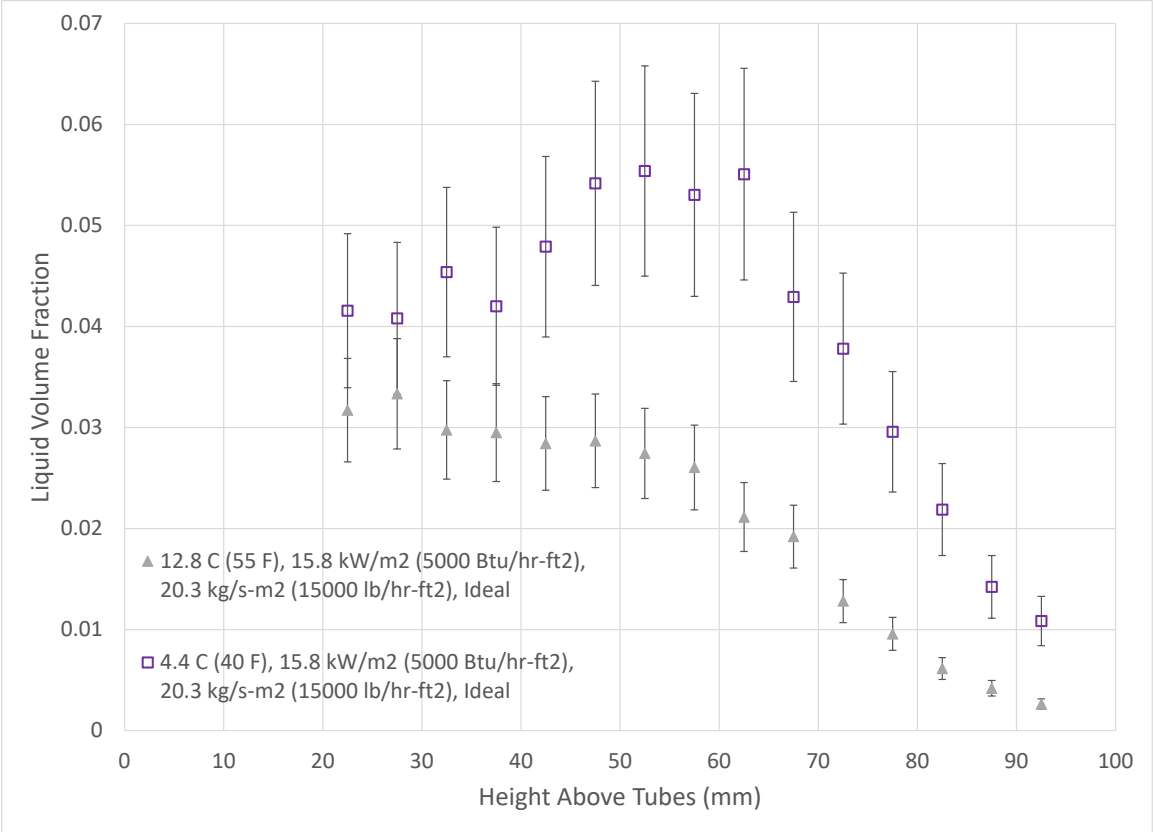

Figure 12: Liquid volume fraction versus height for 15.8 kW/m^2 (5000 Btu/hr-ft^2), 20.3 kg/s-m^2 (15000 lb/hr-ft^2) with 50 mm lens for both 4.4 ^{o}C (40 F) and 12.8 ^{o}C (55 F)

Figure 12 shows the effect of temperature on liquid fraction. Saturated R-123 at 12.8 ^{o}C (55 F) has a vapor density of 3.76 kg/m^3 (0.234 lb/ft^3), whereas the density at 4.4 ^{o}C (40 F) is 2.70 kg/m^3 (0.168 lb/ft^3), a decrease of nearly 40%. Correspondingly, the vapor velocities could be nearly 40% lower for the higher temperature condition This results in more liquid higher up in the headspace for the lower temperature condition as can clearly be seen up to 60 mm above the tube..

Though the results for the higher mass fluxes for R-123 cannot be used for the ideal or flooded cases, the dryout cases are shown in Figure 13. A significant difference is shown between the two heat flux cases at the 40.7 kg/s-m^2 (30000 lb/hr-ft^2) mass flux, with the lower heat flux of 15.8 kW/m^2 (5000 Btu/hr-ft^2) showing more liquid higher up in the headspace than the higher heat flux condition of 31.5 kW/m^2 (10000 Btu/hr-ft^2). This is due to there being less liquid, and thus more vapor, in the top of the bundle to achieve the

lower heat flux. This increased vapor in turn increases the velocity of the vapor/liquid mixture exiting between the top tubes of the bundle.

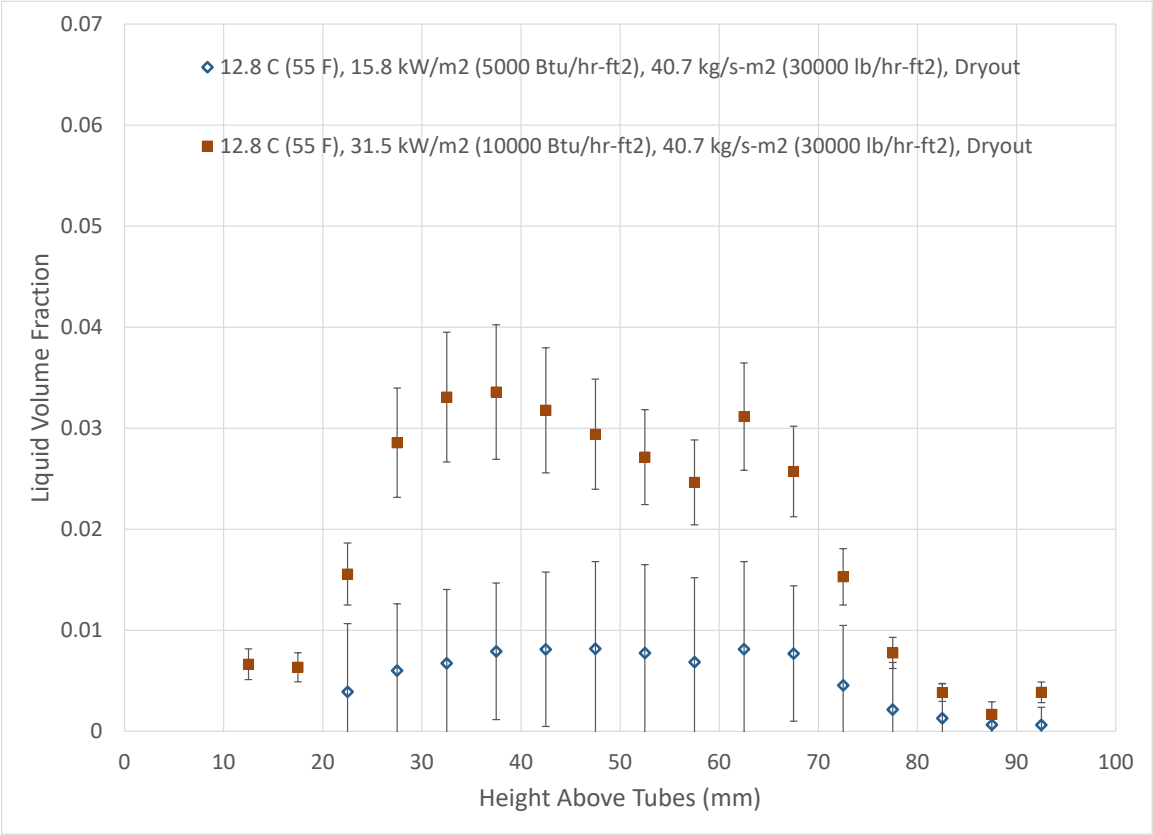

Figure 13: Liquid volume fraction versus height for 12.8 °C (55 F) at dryout condition with 50 mm lens for varying heat flux

Summary and discussion

Two dominant mechanisms are thought to generate the liquid droplets: 1) vapor shear and 2) surface tension dominated wave action. For R-123, due to the high liquid-vapor density ratio, shear is likely the dominant factor due to the high velocities seen at the top of the bundle. We can identify two major flow regions within the headspace based on the expected vapor velocities. First, the maximum velocity occurs in the gaps between tubes at the highest point in the tube bundle. For a saturation temperature of 4.4 C (40 F), this velocity could be as high as 15 m/s. The second regime is at a higher point in the headspace where the velocity jets have dissipated and the flow is uniform and slower. These expected velocities can be used to determine corresponding terminal droplet sizes, which gives a static picture of the expected size

distribution. Figure 14, for example, shows that at 20.4 kg/m^2 s (15000 lb/hr-ft^2) droplets of 2500 microns in size could be entrained at the just above the bundle, but that higher in the headspace droplet sizes should be under 200 micron.

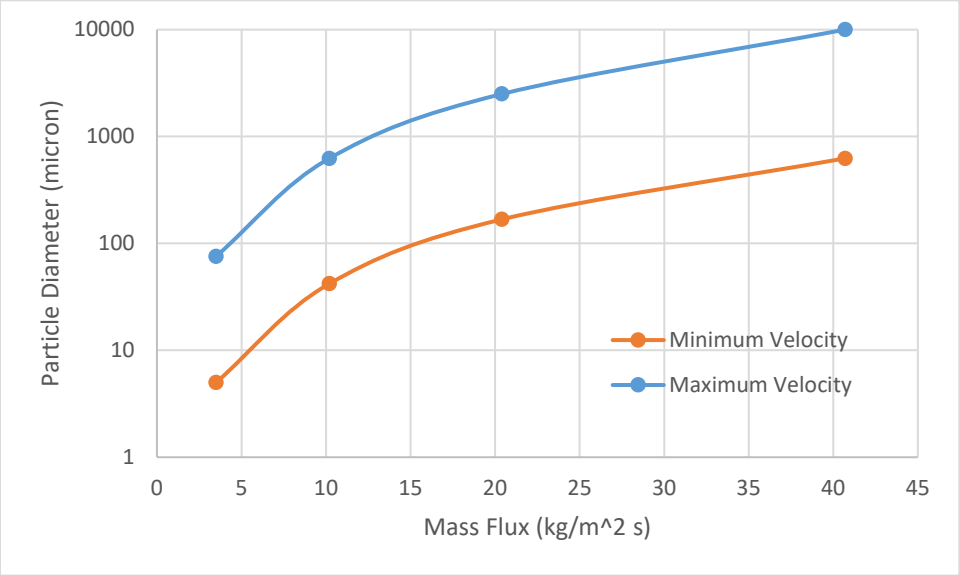

Figure 14: Particle size for maximum and minimum terminal velocity in bundle at 12.8 C (55 F)

The disparity in velocities makes the headspace act as a separation chamber, whose effectiveness is dependent on flow conditions and physical arrangement. As can be seen from Figures 11, 12, 13, and 8, mass flux, liquid level, saturation temperature, and heat flux are all strong actors on the liquid distribution in the headspace, with each's effectiveness seemingly being in that order from most to least. It can be seen that, at least with R-123, a headspace of 100 mm (4 inch) is not sufficient to separate out even moderate sized droplets for mass fluxes above 15.8 kg/s-m2 when there is no decrease in velocity in the headspace.

To that end, it would seem necessary when operating at mass fluxes of 15.8 kg/s-m^2 or more to take the velocity and height considerations in mind. The bundle used in these experiments had a constant-area headspace. As such, vapor velocity in the headspace was constant as height increased, so any droplets below the minimum terminal velocity size would be carried out. An expansion of the walls (increase in cross-sectional area) would have decreased velocities and improved the ability to separate out droplets. The distribution plate located 140 mm [5.5 inch] above the tube bundle both caught and removed droplets, as a measurable temperature drop was observed across the plate. As such, a physical screen or baffle can also

serve to improve separation. Unfortunately for this experiment, the baffle also trapped droplets that would have escaped that instead ran down the sight glass.

Conclusion

The headspace in a flooded evaporator can be a complex environment. These spaces typically also act as separation spaces that prevent harmful liquid droplets from reaching the compressor. A system was built to characterize the droplet distribution in the headspace above a tube-bundle evaporator for low-pressure refrigerant R-123. A dual-pulsed Nd:YAG laser and camera system in a shadowgraphy arrangement was used to capture images of the headspace and software was used to recognize and match droplets from the images.

The system conditions were varied such that the evaporator experienced mass fluxes from 3.5 to 40.7 kg/s-m^2 (2250 to 30000 lb/hr-ft^2), top-rows heat fluxes from 5.3 to 31.5 kW/m^2 (1700 to 10000 Btu/hr-ft^2), and outlet saturation temperatures of 4.4 and 12.8 °C (40 and 55 F). The level of the liquid in the evaporator were varied such that the top rows went from flooded to dryout.

Results were presented and discussed, with a headspace liquid volume fraction equation developed. Liquid distribution in the headspace was found to be a strong function of all varied properties, particularly mass flux, liquid level, and saturation temperature. The high vapor velocities of R-123 make it particularly difficult to separate liquid droplets that escape the tube bundle and flow out of the evaporator, though changes to the headspace that induce a reduction in velocity, physical blockage of escaping droplets, or induce a drop in pressure may be beneficial.

Nomenclature

A_c	=	total cross-sectional area
$A_{tube,o}$	=	single tube outer area
$c_{p,w}$	=	specific heat of water
$\overline{D}_i$	=	mean droplet diameter per bin
G	=	mass flux
H	=	bin height

$h_{pb,inlet}$ = preboiler inlet refrigerant enthalpy

$h_{ts,outlet}$ = bundle test section outlet refrigerant enthalpy

$\dot{m}_r$ = refrigerant mass flow rate

$\dot{m}_w$ = water mass flow rate per tube

n_i = droplet count per bin

ϕ_i = liquid volume fraction per bin

q_{bundle} = total bundle heat

q_{pb} = preboiler heat

q_{tube} = single tube heat transfer

$q"_{tube}$ = single tube outer heat flux

T = water temperature

$V_{l,total,i}$ = total liquid volume per bin

W = bin width

References

Castrejón-García, R., J. R. Castrejón-Pita, G. D. Martin and I. M. Hutchings (2011). "The shadowgraph imaging technique and its modern application to fluid jets and drops." Revista Mexicana de Fisica **57**(3): 266-275.

Cheng, L., G. Ribatski and J. R. Thome (2008). "Two-phase flow patterns and flow-pattern maps: Fundamentals and applications." Applied Mechanics Reviews **61**(1-6): 0508021-05080228.

Dai, Z., W. H. Chou and G. M. Faeth (1998). "Drop formation due to turbulent primary breakup at the free surface of plane liquid wall jets." Physics of Fluids **10**(5): 1147-1157.

Eckels, S. and J. Schlup (2017). Two phase flow visualization in evaporator tube bundles using experimental and numerical techniques. 2nd Thermal and Fluids Engineering Conference and 4th International Workshop on Heat Transfer. Las Vegas, ASFTE. **TFEC-IWHT2017-18318**.

Gorgy, E. and S. Eckels (2013). "Convective boiling of R-134a and R-123 on an enhanced tube bundle with standard pitch, RP-1316." HVAC&R Research **19**(2): 193-206.

Gorgy, E. and S. Eckels (2016). "Convective boiling of R-134a on enhanced-tube bundles." International Journal of Refrigeration **68**: 145-160.

Grant, I. D. R. and D. Chisholm (1979). "TWO-PHASE FLOW ON THE SHELL-SIDE OF A SEGMENTALLY BAFFLED SHELL-AND-TUBE HEAT EXCHANGER." J Heat Transfer Trans ASME **101**(1): 38-42.

Hay, K. J., Z. C. Liu and T. J. Hanratty (1998). "A backlighted imaging technique for particle size measurements in two-phase flows." Experiments in Fluids **25**(3): 226-232.

Kashdan, J. T., J. S. Shrimpton and A. Whybrew (2003). "Two-phase flow characterization by automated digital image analysis. Part 1: Fundamental principles and calibration of the technique." Particle and Particle Systems Characterization **20**(6): 387-397.

Kondo, M. and K.-i. Nakajima (1980). "Experimental investigation of air-water two phase upflow across horizontal tube bundles - 1. flow pattern and void fraction." Bulletin of the JSME **23**(177): 385-393.

Patruno, L. E., P. A. Marchioro Ystad, J. M. Marchetti, C. A. Dorao, H. F. Svendsen and H. A. Jakobsen (2010). "Liquid entrainment from a wetted wire exposed to a high gas flow rate in cross flow." Chemical Engineering Science **65**(24): 6397-6406.

Robinson, D. M. and J. R. Thome (2004). "Local bundle boiling heat transfer coefficients on a turbo-BII HP tube bundle (RP-1089)." HVAC and R Research **10**(4): 441-457.

Ulbrich, R. and D. Mewes (1994). "Vertical, upward gas-liquid two-phase flow across a tube bundle." International Journal of Multiphase Flow **20**(2): 249-272.

van Rooyen, E., F. Agostini, N. Borhani and J. R. Thome (2012). "Boiling on a tube bundle: Part I --Flow visualization and onset of dryout." Heat Transfer Engineering **33**(11): 913 - 929.

Van Rooyen, E. and J. R. Thome (2013). "Pressure drop data and prediction method for enhanced external boiling tube bundles with R-134a and R-236fa." International Journal of Refrigeration **36**(6): 1669-1680.

Van Rooyen, E. and J. R. Thome (2014). "Flow boiling data and prediction method for enhanced boiling tubes and tube bundles with R-134a and R-236fa including a comparison with falling film evaporation." International Journal of Refrigeration **41**: 60-71.